Journal of Materials Chemistry A

ROYAL SOCIETY OF CHEMISTRY

PAPER

View Article Online
View Journal | View Issue



Cite this: J. Mater. Chem. A, 2025, 13, 10126

# High-performance hydrogen evolution reaction by $ReS_2/TiO_2$ hollow microcones created through microwave-hydrothermal consecutive synthesis†

Yoonsun Choi,‡ Geonwoo Kim,‡ Dongbeom Kim, Kyu-Su Kim, Junhyeok No, In-Ho Baek, Sang-Mun Jung, * Yong-Tae Kim * and Unyong Jeong *

Received 10th February 2025
Accepted 27th February 2025

DOI: 10.1039/d5ta01077b

rsc.li/materials-a

There is a need to develop a high-performance and low-cost hydrogen evolution reaction (HER) catalyst without noble metal. Transition metal dichalcogenides are some of the most promising catalytic materials, and rhenium disulfide ($ReS_2$) emerges as a favorable material due to its unique structural properties. However, $ReS_2$ is still lacking in research for effective catalytic performance; especially, increasing the electrochemical surface area has not been investigated. Herein, we present a 3D-structured $ReS_2/TiO_2$ catalyst with a high electrochemically active surface area (ECSA) obtained through a simple two-step process: (i) formation of $TiO_2$ hollow microcones by microwave treatment and $ReS_{2-x}$ coating and (ii) $ReS_2$ nanowall formation by a hydrothermal process. The microconical structure of the catalyst obtained *via* the two-step process significantly improved the HER activity of $ReS_2$, exhibiting a low overpotential (61 mV), and a large ECSA (3652 $cm^2$) with negligible degradation after 10 000 cycles of potential scanning and for 72 h of chronopotentiometric measurements at a current density of 500 mA $cm^{-2}$, which is a superior result compared to previously reported $ReS_2$-based HER catalysts.



## Introduction

Hydrogen is a promising energy source in consideration of energy depletion and global warming due to its high energy efficiency and eco-friendly product after use.[1] Green hydrogen evolution reaction (HER) based on water electrolysis has been considered as a clean solution to environmental problems.[2] As HER consumes a large amount of electrical energy and uses only the surfaces of the catalysts, synthesis of efficient and noble metal-free catalysts is essential for practical hydrogen production.[3–5] Transition metal dichalcogenides (TMDCs) have received much attention as HER catalysts due to the high surface area resulting from the layered structure and their earth-abundance.[6–10] Rhenium disulfide ($ReS_2$), as an emerging TMDC member, is a candidate material for HER on account of its unique chemical and electronic properties: weak interlayer coupling,[11] stable distorted 1T-phase unlike other TMDCs,[12] low ion diffusion barrier,[13] and large active site exposure.[14] There have been studies on controlling the HER performance of $ReS_2$, by regulating the internal structures through vacancy-engineering,[15] formation of grain boundaries,[16] and designing superlattices. Zhao *et al.* compared HER catalytic performances while varying the edge density and the length of pure $ReS_2$ under various synthetic conditions.[17] Nonetheless, pure $ReS_2$ still did not reach performance levels comparable to those of noble metals. Recently, doping and decoration of $ReS_2$ with heterogeneous elements have been explored to improve the HER performance. Kim *et al.* presented a Pt/$ReS_2$ hybrid HER catalyst, in which Pt nanoclusters were impregnated in $ReS_2$ nanoflowers.[18] They reported an excellent overpotential (20 mV at 10 mA $cm^{-2}$) and a high electrochemical surface area (4.07 $cm^2$). Liu *et al.* doped fluorine in $ReS_2$ through post-fluorination.[19] They found that F dopants accelerated the charge transfer and increased the active sites, resulting in a low overpotential (142 mV at 10 mA $cm^{-2}$) and a large electrochemical active surface area (ECSA) of 400 $cm^2$. $ReS_2$ without containing noble metals deserves more extensive studies to achieve high HER performance.

Titanium dioxide ($TiO_2$) has been synthesized in various forms[20–24] and is widely used as an energy-related electrode, such as in electrocatalysis (hydrogen evolution, oxygen evolution, and oxygen reduction),[25–28] photocatalysis,[29] lithium-ion batteries,[30] energy conversion,[31] and energy storage.[32] In water electrolysis, the 3D $TiO_2$ structures have been explored as a supporting body, which expands the surface area to improve the catalytic activity. Nong *et al.* proposed a mesoporous $TiO_2$ crystal by etching $SrTiO_3$ under hydrothermal conditions, and doped it with well-dispersed Ru for HER catalytic application.[21] Chen *et al.* also prepared a porous $TiO_2$ nanotube array through

*Department of Materials Science and Engineering, Pohang University of Science and Technology (POSTECH), Cheongam-ro 77, Namgu, Pohang, 37673, Korea. E-mail: ujeong@postech.ac.kr; yongtae@postech.ac.kr; sangmun0104@postech.ac.kr*

† Electronic supplementary information (ESI) available. See DOI: https://doi.org/10.1039/d5ta01077b

‡ These authors contributed equally.

anodic oxidation and introduced Pt nanoclusters on the array by atomic layer deposition to improve the HER performance.[24] Although the composites of 3D-structured $TiO_2$ and noble metal catalysts have made remarkable advances in performance and durability, preparation of 3D-structured $TiO_2$ has limitations in terms of time, cost, and methodological complexity. In addition, there have been few studies that improved the HER performance only with $TiO_2$ and non-noble metals.

In this paper, we report a unique 3D-structured, noble metal-free, high-performance $ReS_2$ HER catalyst. The catalyst is produced on a Ti fiber felt, creating $ReS_2$ nanowalls on $TiO_2$ hollow microcones generated *in situ* on the Ti felt. We suggest a two-step synthesis: (i) microwave-assisted 3D structuring of $TiO_2$ and $ReS_2$ coating on the surface and (ii) hydrothermal refining of the $ReS_2$ nanowalls to significantly improve the HER performance such as a low overpotential (61 mV at 10 mA $cm^{-2}$), a high ECSA (3652 $cm^2$), excellent cyclic durability (no degradation after 10 000 cycles), and good potential retention (for 72 h at a current density of 500 mA $cm^{-2}$). The mechanism of microcone formation, the chemistry of the crystal structures, and long-term catalytic performances are thoroughly investigated.

## Results and discussion

### Formation of the $ReS_2/TiO_2$ hollow microcones

The two-step synthesis of the hollow $ReS_2/TiO_2$ microcones is depicted in Fig. 1a. Ammonium perrhenate ($NH_4ReO_4$) and thiourea ($SC(NH)_2$) were used as a Re precursor and as a S precursor, respectively. The precursors were dissolved in an ionic material (BMIM:$BF_4$), which acted both as a solvent and as a microwave (MW) absorber. Ti fiber felt was selected as a Ti source and a self-supported electrode. When MW was applied to the Ti felt immersed in the precursor solution for 2 min, $TiO_2$ microcones were created on the surface of the Ti felt, and $ReS_{2-x}$ nanoparticles were coated onto the $TiO_2$ microcones. The hydrothermal (HT) process maintained the microcone structure and generated stoichiometric $ReS_2$ nanowalls. Scanning electron microscopy (SEM) images in Fig. 1b–d exhibit the surface morphologies of (b) the bare Ti felt, (c) $ReS_2$ (MW), $ReS_{2-x}/TiO_2$ created by the MW process, and (d) ReS2 (MW-HT), $ReS_2/TiO_2$ created by the MW-HT consecutive process. The bare Ti felt did not have any protruding structures on the surface. The average bottom diameter of the microcones of the $ReS_2$ (MW) specimen was about 5 μm. Based on energy-dispersive X-ray spectroscopy (EDS), the average stoichiometry of $ReS_2$ (MW) was determined to be $ReS_{1.62}$ (Table S1†), whereas it was stoichiometric ($ReS_{1.97}$) in the $ReS_2$ (MW-HT) specimen. The nanowall structure of $ReS_2$ became prominent after the HT process (Fig. 1d).

MW treatment can electromagnetically agitate ionic species. For instance, during the synthesis of $ReS_2$, the Re precursor was ionized to form $NH_4^+$ and $ReO_4^-$. These ions, together with the ionic material (BMIM:$BF_4$), could absorb MW and cause volumetric heating,[33] which is essential for rapid synthesis. Because the solubility and degree of ionization of the precursor depend on ionic molecules, proper combination of the precursors and ionic molecules is crucial for the MW-assisted synthesis. Various materials (ionic molecules, metal precursors) were explored to find out the appropriate combinations. Specifically, BMIM:$BF_4$ actively generated the $TiO_2$ microcones (Fig. S1a†); thus we used it in this study. Presence or absence of $SC(NH)_2$ did not affect the formation of the microcones, whereas the transition metal precursors affected it considerably. The microcones could be formed using various Re and Mo precursors ($NH_4ReO_4$, $ReCl_5$, $(NH_4)_2MoO_4$, $MoO_2(acac)_2$, $MoCl_5$, and $(NH_4)_2MoS_4$) (Fig. S1b†). However, the microcones were not formed by using other transition metal precursors ($WCl_4$, $ZrCl_4$, $NbCl_5$, $FeCl_2 \cdot 4H_2O$, $CoCl_3$, and $CrCl_3$) (Table S2†), and no 3D structures were found on the Ti felt surface, which is because they have a low decomposition degree under MW heating in BMIM:$BF_4$.

To confirm the decomposition degree and reactivity of each precursor, the amount of metal oxides formed from the Re, Mo, and W precursors in the ionic solution by the MW process, in the absence of $SC(NH)_2$, was compared. The W precursor was selected as a representative precursor with a low reactivity. After 2 min of MW reaction in the ionic solution, metal oxide nanoparticles were deposited on the Ti felt, and the remaining amount was dispersed in the reaction solution (Fig. S2†). The dispersed metal oxide nanoparticles in the solution were centrifuged and washed with pure ethanol twice. The collected nanoparticles were dispersed again in fresh ethanol (5 mL). Inductively coupled plasma mass spectroscopy (ICP-MS) was conducted with 5 mL of this dispersion to quantify the amount of metal ions in the dispersion. The amounts of ions of Re (14.1 μmol) and Mo (50.6 μmol) were more than 10 times greater than that of W ions (1.9 μmol) (Table S3†). This result obviously indicates that Re and Mo precursors could be decomposed actively during the MW process, unlike other metal precursors such as the W precursor. In addition, as Re was better deposited on the Ti felt than Mo, the amount of Re remaining in the solution was less than that of Mo. This is why the microcones synthesized using the Re precursor were larger and denser than when Mo precursor was the reactant.

### Characterization of the $ReS_2/TiO_2$ hollow microcones

Fig. 2a–d characterize the microcones peeled off from the Ti felt of $ReS_2$ (MW-HT). The inside of the microcone was hollow (Fig. 2a). The elemental mapping (Fig. 2b) and the SEM image (Fig. S3†) reveal that the inside surface was coated with $ReS_2$ as well as the outside surface. The transmission electron microscopy (TEM) image in Fig. 2c shows the $ReS_2$ nanowalls grown on $TiO_2$ which were collected by ultrasonication for 1 h. The high-resolution TEM (HR-TEM) image in Fig. 2d shows the 0.62 nm lattice spacings and 0.34 nm spacing which correspond to the (001) plane of $ReS_2$ and the anatase $TiO_2$ (101) plane.

X-ray diffraction (XRD) patterns of the bare Ti felt, $ReS_2$ (MW) specimen, and $ReS_2$ (MW-HT) specimen are exhibited in Fig. 2e. The peaks corresponding to anatase $TiO_2$ are marked with solid triangles. New peaks were generated at 25.4° and 47.8° after the MW process and they were maintained after the MW-HT process, indicating new generation of anatase $TiO_2$ on the Ti felt surfaces by MW and maintenance of the crystals during the

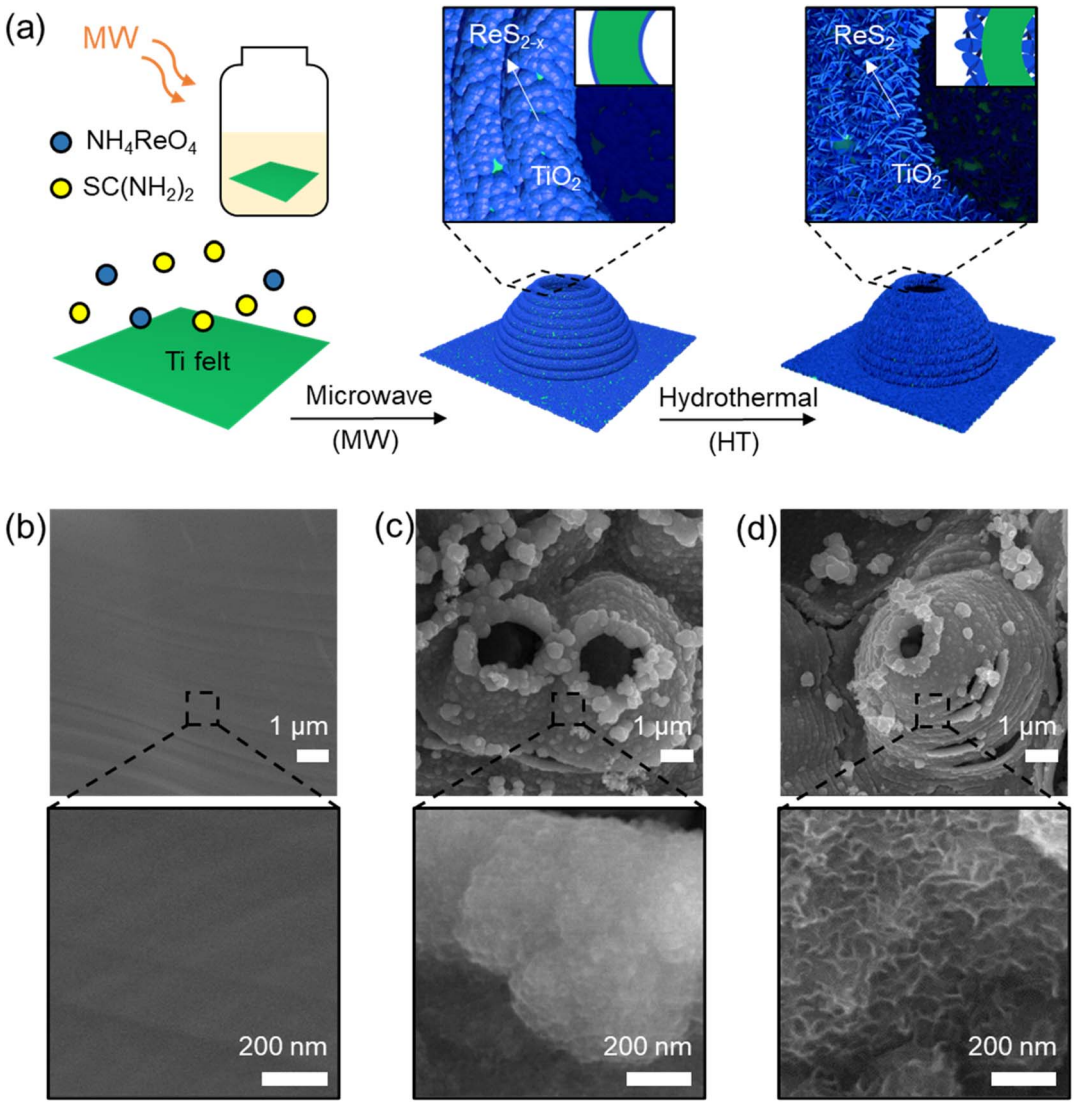


Fig. 1 Morphological evolution of the $ReS_2/TiO_2$ microcones. (a) Illustration of the $ReS_2/TiO_2$ microcones with $ReS_2$ nanowalls on the surfaces. The structure was synthesized by consecutive processes of microwave (MW) treatment and hydrothermal synthesis. The insets magnify the top of the microcones corresponding to the processes. FE-SEM images of bare Ti felt (b), $ReS_{2-x}/TiO_2$ (c), and $ReS_2/TiO_2$ (d).

HT process. The peak of the $ReS_2$ nanowalls was not observed due to the relatively small amount compared to Ti and $TiO_2$. Fig. 2f shows the Raman spectra of the bare Ti felt, $ReS_2$ (MW) specimen, and $ReS_2$ (MW-HT) specimen. Raman peaks from pure $ReS_2$ crystalline powder are compared, denoted with hollow triangles. For the pure $ReS_2$, the peaks at 148 $cm^{-1}$ and 204 $cm^{-1}$ are assigned to the in-plane ($E_g$) and out-of-plane ($A_g$-like) vibration modes of $ReS_2$, respectively. The $ReS_2$ peaks appeared after the MW process, and they became more prominent after the HT process, implying that the crystal structure of $ReS_2$ was refined by the HT process. The anatase $TiO_2$ peaks are marked with solid triangles. The spectrum of bare Ti did not have peaks corresponding to crystalline $TiO_2$. After the MW process, the $TiO_2$ peaks appeared and remained the same after the HT process.

X-ray photoelectron spectroscopy (XPS) also confirmed the formation of $ReS_2$. Fig. 3a and b compare the Re 4f XPS spectra of $ReS_2$ obtained only by HT (Fig. 3a) and by the MW-HT two-step process (Fig. 3b). The $ReS_2$ (HT) specimen contained 32% oxidation states of Re in the $Re_2O_7$ phase. In contrast, the $ReS_2$ (MW-HT) specimen showed a negligible fraction of oxidized Re, which indicates that the $ReS_2$ phase created an interface with the $TiO_2$ support layer without the presence of an oxidized Re layer. On the basis of the results, $ReS_2$ is considered as the active site for HER, while $TiO_2$ is a material serving as a support. The HER mechanism for $ReS_2$ has been well investigated already in many theoretical studies.[34–36] The activity of the catalyst prepared in this study can be characterized according to the reported theoretical results.

We analysed X-ray absorption near edge structure (XANES) spectra to confirm the changes in the local electronic structure of the $ReS_2$ (MW-HT) catalyst (Fig. 3c). Typically, the white line intensity or area of XANES spectra for platinum group metal (PGM) correlates with the oxidation state of a metal, where

 

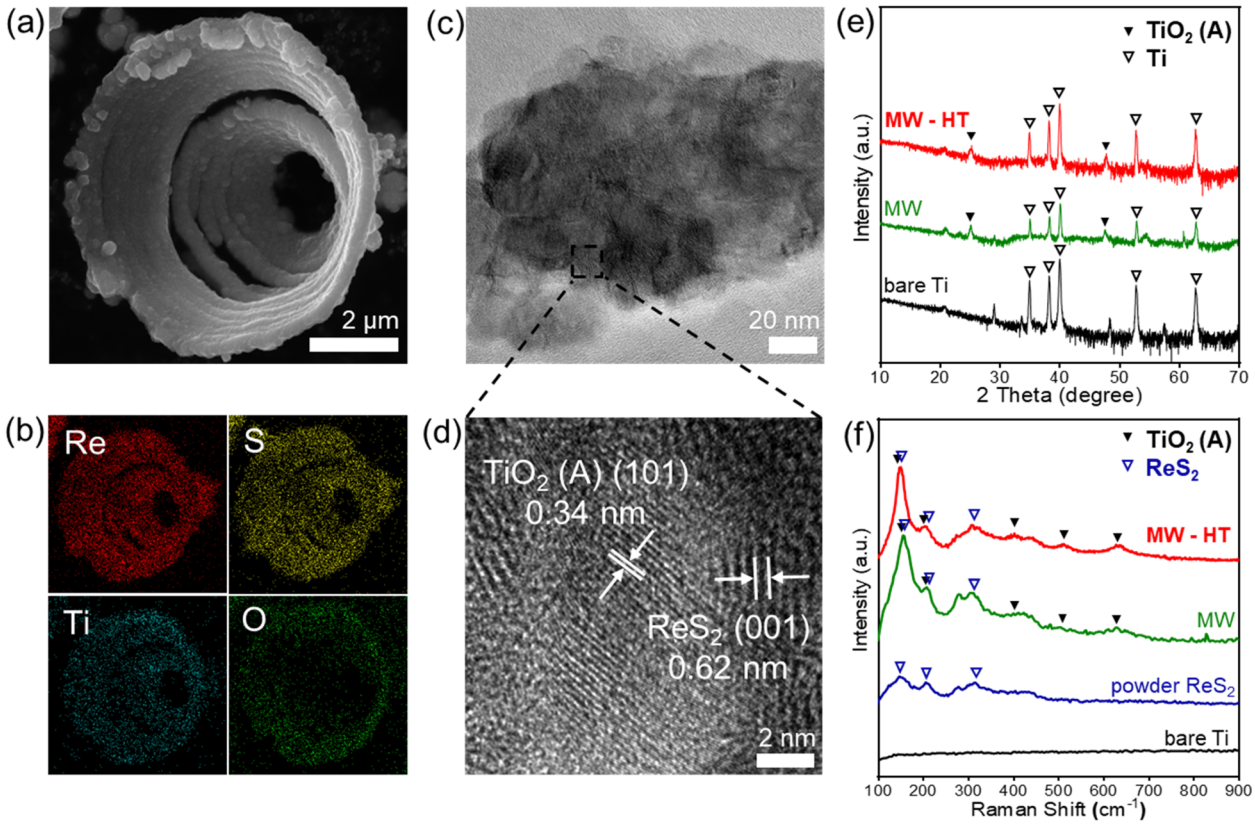


Fig. 2 Characterization of the $ReS_2/TiO_2$ microcones obtained by the MW-HT consecutive process. (a) SEM image and (b) elemental mappings of the $ReS_2/TiO_2$ microcone. (c) TEM and (d) HR-TEM images taken from $ReS_2/TiO_2$. The spacings of $ReS_2$ (001) and anatase $TiO_2$ (101) are indicated. (e) Comparison of XRD patterns and (f) Raman spectra of the $ReS_2$ (MW) specimen and $ReS_2$ (MW-HT) specimen (powder $ReS_2$ was a reference, and bare Ti was the background).

higher intensity or area indicates a higher oxidation state.[18,37] The Re $L_3$-edge spectra in Fig. 3c reveal that the white line in the Re $L_3$-edge adsorption edge for $ReS_2$ (MW-HT) catalyst decreased compared to the $ReS_2$ (HT) catalyst, indicating lower oxidation state in the $ReS_2$ (MW-HT) catalyst. The XANES results were consistent with the XPS results.

The $ReS_2$ growth mechanisms are illustrated for the HT process on Ti (Fig. 3d) and for the MW-HT process on the $TiO_2$

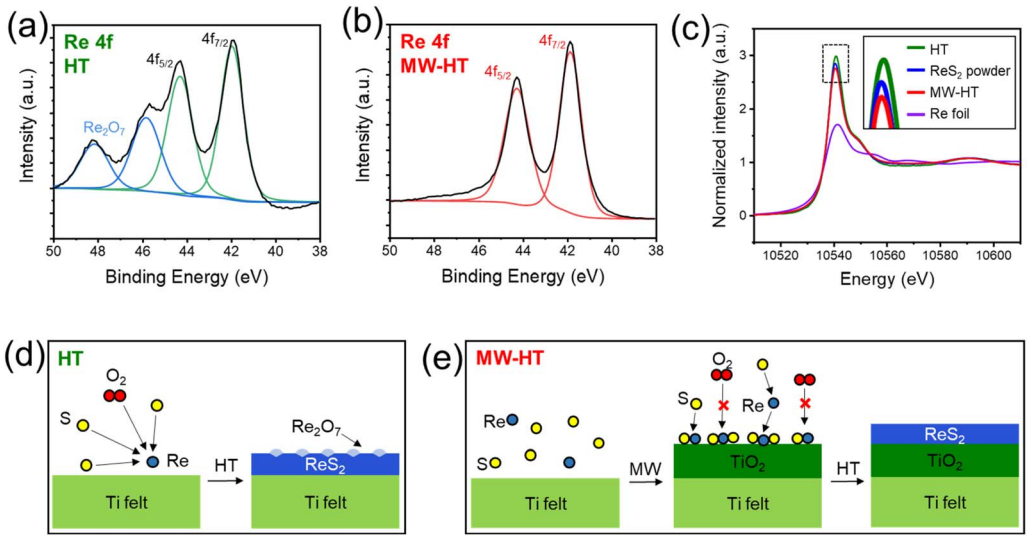


Fig. 3 Difference in the structural evolution when only the HT process was applied and when the MW-HT consecutive process was applied. Re 4f XPS spectra of the $ReS_2$ (HT) (a) and $ReS_2$ (MW-HT) (b) specimens. (c) XANES Re $L_3$-edge spectra of $ReS_2$ (MW-HT) and $ReS_2$ (HT) ($ReS_2$ powder and Re foil were references). Illustration for the competitive oxidation and sulfurization for $ReS_2$ (HT) (d) and $ReS_2$ (MW-HT) (e) specimens.

microcones (Fig. 3e). In the HT process (12 h) without prior surface coating with $ReS_{2-x}$, the S elements decomposed from the precursor should compete with oxygen for the reaction with Re; therefore, $Re_2O_7$ could exist to a significant degree. Conversely, in the MW-HT consecutive process, as the $ReS_{2-x}$ coating layer on the $TiO_2$ surfaces provided plenty of Re–S bonds, bond breaking by oxygen to form oxides is not relevant during the later HT step. Thus, there were no Re oxides on the $TiO_2$ microcones. Because Re oxides interfere with the catalytic reaction on the surface of $ReS_2$, prevention of Re oxidation is critical for HER performance.[38]

### Formation mechanism of the $ReS_2/TiO_2$ hollow microcones

SEM images in Fig. 4a exhibit the temporal evolution of the $ReS_{2-x}/TiO_2$ microcones during the MW process. The evolution of the conical structure is schematically described in Fig. 4b. Two events occurred in parallel during the MW process: (i) formation of a thick $TiO_2$ layer (~500 nm) by oxidation of Ti and (ii) deposition of Re on the surface of the $TiO_2$ layer. Delamination occurs along the cracks in the $TiO_2$ layer or at the inherent defects on the surface of the commercial Ti fiber felt. The conical structures with a diameter of 1 μm were formed in 45 s of the MW delamination and the $ReS_{2-x}$ layer covered the outer surface of the $TiO_2$ microcones within 60 s, which was confirmed through the SEM study (Fig. S4†). The top of each microcone began to be perforated as the size of the microcone increased. The bottom dimension of the microcone reached 5 μm in 90 s of MW treatment and was saturated. All the microcones were perforated within 120 s of MW treatment. The top opening of the microcones allowed deposition of $ReS_{2-x}$ on their interior surfaces. In addition, the opening enabled formation of new $TiO_2$ on the Ti felt

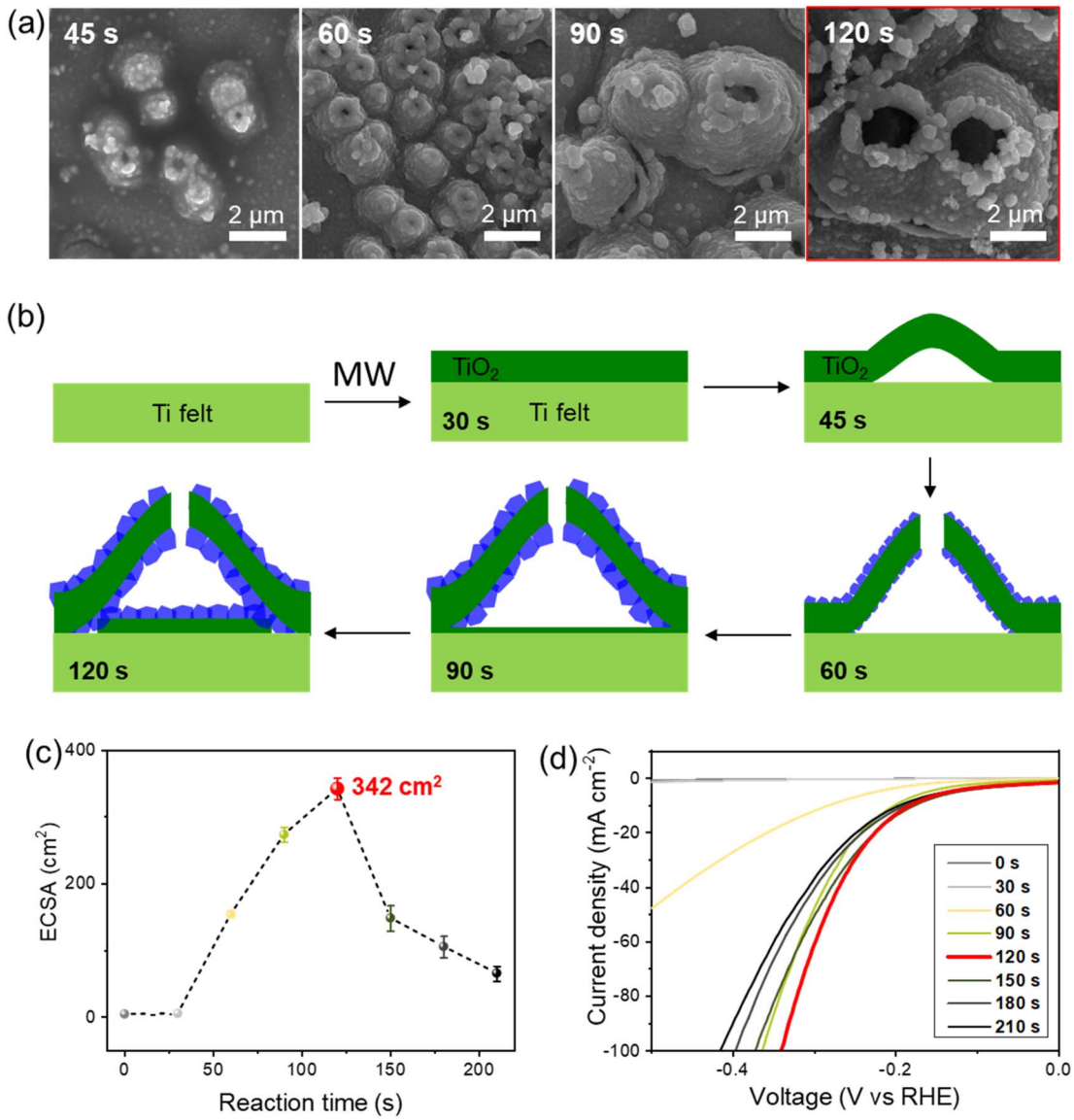


Fig. 4 Temporal process of microcone formation and the catalytic performance of $ReS_2$ (MW) depending on the MW reaction time. (a) SEM images at each growth stage. (b) Schematic description for the growth stages of the $ReS_2$ (MW) during the MW process. Changes of the ECSA (c) and the LSV curves (d) depending on the MW reaction time (from 0 s to 120 s).

 

area corresponding to the bottom of the microcones, on which $ReS_{2-x}$ could be further deposited. The microcones began to be peeled off from the Ti felt in 150 s of MW treatment and large fractions were peeled off at 180 s (Fig. S5†). Therefore, we set the time of the MW process at 120 s to prevent loss of catalyst. The same vertical structure was also obtained on a Ti foil by applying the same MW process (Fig. S6†).

The unique 3D morphology resulted in gradual enhancement of ECSA according to the MW process time from 3.4 $cm^2$ (0 s) to 4.5 $cm^2$ (30 s), 154 $cm^2$ (60 s), 273 $cm^2$ (90 s), and 342 $cm^2$ (120 s) (Fig. 4c). Because the microcones were delaminated from the Ti felt by further MW process, the ECSA curve showed a decreasing trend with MW time, for instance 148 $cm^2$ in 150 s. In line with the ECSA trend, the HER activity showed the best performance at 120 s of MW treatment, with the lowest overpotential ($\eta = 181$ mV) at 10 mA $cm^{-2}$ current density (Fig. 4d).

### Electrocatalytic HER performance of the catalysts

The HER performance of the $ReS_2$ (MW-HT) catalyst was measured using a three-electrode system in $H_2$-saturated 0.1 M $HClO_4$ electrolyte at room temperature. The potential associated with zero current was recorded as the potential of Ag/AgCl (Fig. S7†), and then all electrode potentials were noted against the reversible hydrogen electrode (RHE).[39] The HER polarization curves were acquired using linear sweep voltammetry (LSV). The fifth scan was chosen for the LSV curve in each sample, and all the acquired data were calibrated with a RHE. The $ReS_2$ (MW) catalyst showed a relatively poor catalytic performance ($\eta = 181$ mV at 10 mA $cm^{-2}$) (Fig. 5a). The $ReS_2$ (HT) catalyst showed slightly better performance ($\eta = 140$ mV at 10 mA $cm^{-2}$), but still much lower than the performance of a reported Pt/C catalyst ($\eta = 30$ mV at 10 mA $cm^{-2}$).[18] The $ReS_2$ (MW-HT) catalyst showed a remarkable improvement of the HER performance, reaching 61 mV at 10 mA $cm^{-2}$.

We measured the double-layer capacitance in cyclic voltammograms and compared the calculated ECSA (Fig. 5b). The ECSA of $ReS_2$ (MW-HT) was 3652 $cm^2$, which was in contrast to the values of bare Ti (3.4 $cm^2$), $ReS_2$ (MW) (342 $cm^2$), and $ReS_2$ (HT) (1302 $cm^2$). The electrocatalytic properties of the same specimens were characterized by electrochemical impedance spectroscopy (EIS) analysis (Fig. 5c). The diameter of the semicircles in the Nyquist plot represents the charge-transfer resistance ($R_{ct}$), which has a significant effect on the reaction kinetics. The value of $R_{ct}$ for $ReS_2$ (MW-HT) was lowest ($R_{ct} = 7$ Ω) at $\eta = 100$ mV, compared to $ReS_2$ (HT) ($R_{ct} = 17$ Ω), $ReS_2$ (MW) ($R_{ct} = 63$ Ω), and bare Ti ($R_{ct} = 1500$ Ω). Quantitative HER kinetics was compared with the Tafel slope (Fig. S8†). The Tafel slope of $ReS_2$ (MW-HT) was 153 mV $dec^{-1}$, which was lower than that of $ReS_2$ (HT) (160 mV $dec^{-1}$) and $ReS_2$ (MW) (185 mV $dec^{-1}$). These results indicate that the superior HER activity of $ReS_2$ (MW-HT) is attributed to the high ECSA, fast charge-transfer rate and reaction kinetics.

Long-term durability is a crucial performance indicator for water electrolysis (Fig. 5d). We conducted an accelerated degradation test (ADT) for the $ReS_2$ (MW-HT) catalyst. After 10 000 voltammetry cycles in the range of −0.2 to 0.1 V (*vs.* RHE), the catalyst showed a negligible negative shift (≤2 mV at 10 mA $cm^{-2}$). Furthermore, the $ReS_2$ (MW-HT) catalyst showed excellent HER stability for 72 h at a high current density of 500 mA $cm^{-2}$, with a negligible activity loss. The amount of dissolved Re in the electrolyte, analysed by ICP-MS, was approximately 44 ppb, indicating a negligible level. XPS analysis further confirmed the high HER stability of $ReS_2$ (MW-HT) (Fig. S9†), displaying no changes

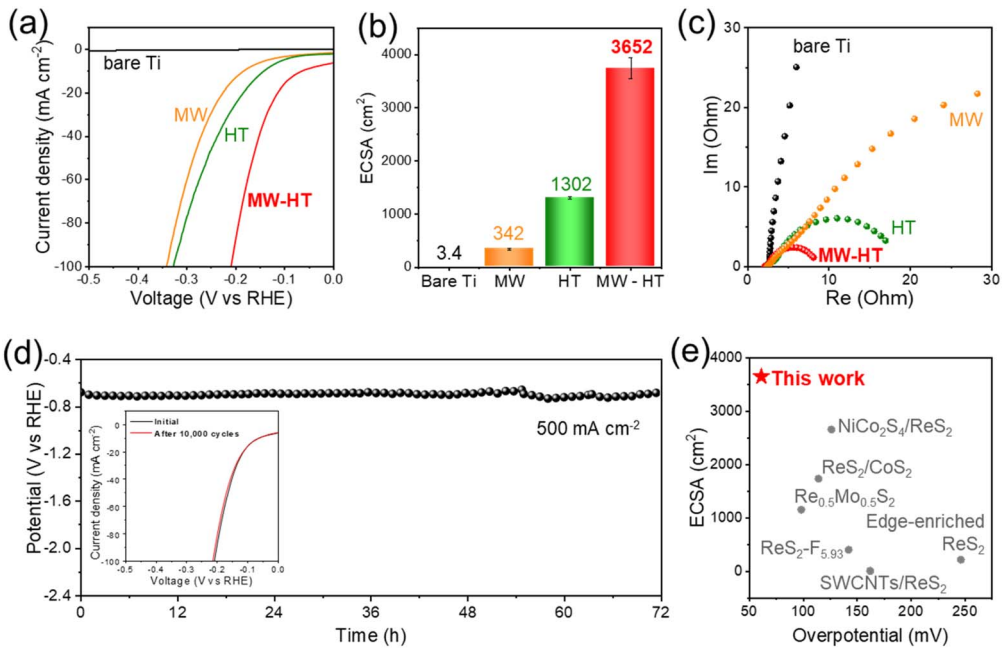


Fig. 5 HER performance of the catalysts. (a) LSV polarization curves, (b) ECSA calculated from the double-layer capacitance, and (c) Nyquist plots. (d) Cyclic voltammetry cycles and chronopotentiometry. (e) HER performance comparison with previously reported Pt-free $ReS_2$-based catalysts in acidic media.

in the chemical state after the chronopotentiometry. The increased intensity of the H–O peak in the O 1s spectrum was attributed to the water-based nature of the HER process.

The $ReS_2$ (MW-HT) catalyst investigated in this study exhibited superior HER performance compared with that of previously reported $ReS_2$-based Pt-free electrodes in acid media. Fig. 5e and Table S4† compare the performances with literature values.[10,17,19,40–42] The performances of the $ReS_2$ (MW-HT) catalyst were comparable with the recent values obtained for $ReS_2$-based HER catalysts containing Pt in acidic media (Table S5†). On the basis of the results, we can conclude that our catalytic electrode had a low overpotential and a high ECSA in addition to excellent stability.

# Experimental

## Chemicals

All the chemicals were of analytical grade and used as received without further purification. Ammonium perrhenate ($NH_4ReO_4$), thiourea ($CH_4N_2S$), hydroxylamine hydrochloride ($NH_2OH \cdot HCl$), 1-butyl-3-methylimidazolium tetrafluoroborate (BMIM:$BF_4$), and oxalic acid ($(COOH)_2 \cdot 2H_2O$) were purchased from Sigma-Aldrich. Ethanol was purchased from Daejung Chemicals, Inc. (Korea). Ti fiber felt was purchased from Bekaert.

## Synthesis of $ReS_2$ powder

The $ReS_2$ powder was synthesized using the microwave-irradiation method.[18] 16.8 mg of ammonium perrhenate ($NH_4ReO_4$) and 23.8 mg of thiourea ($CH_4N_2S$) were first dissolved in 2.5 mL of BMIM:$BF_4$ at room temperature. After being stirred for 4 h, the solution was transferred to a 20 mL quartz vial. Subsequently, the solution was heated in a domestic microwave oven at 200 W for 2 min and then allowed to cool to room temperature naturally. The product was washed with water and then ethanol three times using centrifugation. The $ReS_2$ powder was dried at 60 °C for 6 h.

## Synthesis of $ReS_2$ (MW)

Prior to synthesis, the Ti fiber felt substrate was acid-treated with 5 wt% oxalic acid solution at 80 °C for 30 min to remove surface oxide and contaminants.[43] 16.8 mg of ammonium perrhenate ($NH_4ReO_4$) and 23.8 mg of thiourea ($CH_4N_2S$) were first dissolved in 2.5 mL of BMIM:$BF_4$ at room temperature. After being stirred for 4 h, the solution was transferred to a 20 mL quartz vial, and a $1 \times 1$ cm$^2$ part of $1 \times 3$ cm$^2$ Ti felt was immersed into the solution. Subsequently, the solution was heated in a domestic microwave oven at 200 W for 2 min and then allowed to cool to room temperature naturally. The felt was washed with ethanol and then water three times each with vigorous shaking. The $ReS_{2-x}/TiO_2$ on the Ti felt was dried at room temperature for 2 h.

## Synthesis of $ReS_2$ (HT)

134 mg of ammonium perrhenate ($NH_4ReO_4$), 190 mg of thiourea ($CH_4N_2S$) and 104 mg of hydroxylamine hydrochloride ($NH_2OH \cdot HCl$) were dissolved in 20 mL of deionized water under magnetic stirring at room temperature for 30 min. The aqueous solution was transferred to a 50 mL Teflon-lined autoclave, and a $1 \times 1$ cm$^2$ part of $1 \times 3$ cm$^2$ Ti felt was immersed into the solution. The autoclave was sealed and maintained at 220 °C for 12 h. After cooling down to room temperature, the felt was washed with ethanol and then water three times each with vigorous shaking and then dried at room temperature for 2 h.

## Synthesis of $ReS_2$ (MW-HT)

134 mg of ammonium perrhenate ($NH_4ReO_4$), 190 mg of thiourea ($CH_4N_2S$) and 104 mg of hydroxylamine hydrochloride ($NH_2OH \cdot HCl$) were dissolved in 20 mL of deionized water under magnetic stirring at room temperature for 30 min. The aqueous solution was transferred to a 50 mL Teflon-lined autoclave, and a $1 \times 1$ cm$^2$ part of $1 \times 3$ cm$^2$ $ReS_2$ (MW) was immersed into the solution. The autoclave was sealed and maintained at 220 °C for 12 h. After cooling down to room temperature, the felt was washed with ethanol and then water three times each with vigorous shaking and then dried at room temperature for 2 h.

## Structural characterization

The morphology of the synthesized catalyst was observed using field-emission SEM (Hitachi S-4800), TEM (JEOL JEM-2100F) at 200 kV, and high-angle annular dark-field scanning transmission electron microscopy (HAADF-STEM; JEOL JEM-2100F with Cs Corrector) at 200 kV. Powder XRD (Rigaku D/MAX-2500/PC) was performed with Cu K$\alpha$ radiation ($\lambda$ = 1.54 Å). The Raman spectrum was obtained using a micro-Raman spectrometer (Witec Alpha 300 RA Confocal Raman) with a wavelength of 532 nm and a laser spot size of 1 μm. The amounts of Re and S were measured using the SEM instrument equipped with an EDS facility (INCA X-sight 7421, Oxford Instruments). The XANES data at the Re k-edge were obtained at the 7D beamline in the PAL with fluorescence mode. The X-ray beam was monochromated by a Si (111) double crystal, where the beam intensity was reduced by 30% to eliminate higher-order harmonics.

## ICP-MS characterization

The metal ion concentration was measured using ICP-MS (PerkinElmer, NexION 300S). To ensure analysis reliability, calibration curves were obtained by linear fitting of the raw intensities of each element at 1, 5, and 10 ppb before the ion concentration measurements. The electrodes were fully dissolved in aqua regia using an ultrasonic bath, and the ion concentration measurements were conducted by diluting the solution to fit within the calibration curves.

## Electrochemical measurements

All the electrochemical characterizations were performed using an electrochemical workstation (Metrohm Autolab, PGSTAT204). Electrochemical measurements were conducted using a standard three-electrode electrochemical system in 0.1 M $HClO_4$ (Sigma-Aldrich) solution at room temperature. The

 

prepared samples, a graphite rod, and an Ag/AgCl (sat. KCl) were used as the working, counter, and reference electrodes, respectively. The graphite rod was used as the counter electrode to prevent undesirable back reactions and cross-contamination by trace Pt metal species.[44] The calibration of the Ag/AgCl reference electrode was conducted in high-purity (99.999%) $H_2$-saturated 0.1 M $HClO_4$ with a polycrystalline Pt pellet as working electrode.[39,45] Linear sweep voltammetry curves were obtained with sweeping the potential between hydrogen evolution (−100 mV) and oxidation (+100 mV) regions with a scan rate of 1 mV $s^{-1}$, at room temperature. The Tafel plots were replotted to the HER polarization curves as overpotential ($\eta$) *versus* log current density (log$j$) The polarization curves for HER were obtained using $H_2$-saturated 0.1 M $HClO_4$ at a scan rate of 10 mV $s^{-1}$ and the potential was *iR*-corrected with workstation-assisted *iR* drop compensation ($iR$ = 2 Ω). EIS measurements were performed at −0.02 V *vs.* RHE, using a sinusoidal wave with a frequency scan range from $10^5$ to $10^{-1}$ Hz and an amplitude of 10 mV. The measured EIS data were analyzed with the NOVA software package. The $ECSA_{C_{dl}}$ values of the electrodes were calculated by the potential-sweep method in the electrochemical double-layer region.[46,47] The capacitance was measured *via* cyclic voltammetry in a non-faradaic potential range of 0.15 to 0.3 V (*vs.* RHE), using 5 to 400 mV $s^{-1}$. An accelerated durability test was conducted with an extended potential cycling test (10 000 cycles) in the range of −0.2 V to 0.1 V (*vs.* RHE) with a scan rate of 50 mV $s^{-1}$. Chronopotentiometry measurements were also performed with a current density of 500 mA $cm^{-2}$ for 72 h.

## Conclusions

We have synthesized $ReS_2/TiO_2$ composites directly on Ti felt with an ultra-high electrochemical surface area by employing two sequential processes: rapid microwave irradiation and a well-established hydrothermal method. Microconical $TiO_2$ structures with nonstoichiometric $ReS_{2-x}$ fully covering the surface were grown during 2 min of microwave irradiation. Subsequently, the deficient sulfur was replenished to convert $ReS_{2-x}$ to $ReS_2$ through sequential 12 h hydrothermal synthesis. We could identify the growth mechanism of the catalytic materials on 3D $TiO_2$ through microwave treatment. The optimized $ReS_2$ (MW-HT) showed HER catalytic activity with a low overpotential of 61 mV, $R_{ct}$ of 7 Ω, robust durability (showing negligible activity loss after 10 000 cycles of cyclic voltammetry and over 72 h at 500 mA $cm^{-2}$), and an ultra-high electrochemical surface area of 3652 $cm^2$.

## Data availability

The data that support the findings of this study are available from the corresponding author upon reasonable request.

## Author contributions

U. J. and Y.-T. K. conceived the original idea, supervised the work. U. J., Y.-T. K., and S.-M. J. edited the final manuscript. S.-M. J. and I.-H. B. conducted electrochemical measurements. Y. C. and G. K. performed the catalyst synthesis, conducted structural characterizations, and wrote the initial draft. D. K. and J. N. analysed the measured data. K.-S. K. conducted ICP-MS measurements.

## Conflicts of interest

There are no conflicts to declare.

## Acknowledgements

This work was supported by the National Research Foundation of Korea (NRF) grant funded by the Korea government (MSIT) (No. RS-2024-00338686, No. NRF-2022M3H4A1A02074314, No. 2019M3D1A1079306, and No. RS-2025-00554594).

## References

1 M. A. Rosen and S. Koohi-Fayegh, *Energy Ecol. Environ.*, 2016, **1**, 10–29.
2 S.-Y. Ahn, K.-J. Kim, B.-J. Kim, G.-R. Hong, W.-J. Jang, J. W. Bae, Y.-K. Park, B.-H. Jeon and H.-S. Roh, *Renewable Sustainable Energy Rev.*, 2023, **186**, 113635.
3 J. Kim, H. Jung, S.-M. Jung, J. Hwang, D. Y. Kim, N. Lee, K.-S. Kim, H. Kwon, Y.-T. Kim and J. W. Han, *J. Am. Chem. Soc.*, 2020, **143**, 1399–1408.
4 X. Zou and Y. Zhang, *Chem. Soc. Rev.*, 2015, **44**, 5148–5180.
5 Y. Cao, *ACS Nano*, 2021, **15**, 11014–11039.
6 L. Cheng, W. Huang, Q. Gong, C. Liu, Z. Liu, Y. Li and H. Dai, *Angew. Chem., Int. Ed.*, 2014, **53**, 7860–7863.
7 Y. Li, H. Wang, L. Xie, Y. Liang, G. Hong and H. Dai, *J. Am. Chem. Soc.*, 2011, **133**, 7296–7299.
8 I. S. Amiinu, Z. Pu, X. Liu, K. A. Owusu, H. G. R. Monestel, F. O. Boakye, H. Zhang and S. Mu, *Adv. Funct. Mater.*, 2017, **27**, 1702300.
9 X. Wang, Y. Chen, B. Zheng, F. Qi, J. He, Q. Li, P. Li and W. Zhang, *J. Alloys Compd.*, 2017, **691**, 698–704.
10 I. H. Kwak, T. T. Debela, I. S. Kwon, J. Seo, S. J. Yoo, J.-G. Kim, J.-P. Ahn, J. Park and H. S. Kang, *J. Mater. Chem. A*, 2020, **8**, 25131–25141.
11 S. Tongay, H. Sahin, C. Ko, A. Luce, W. Fan, K. Liu, J. Zhou, Y.-S. Huang, C.-H. Ho and J. Yan, *Nat. Commun.*, 2014, **5**, 3252.
12 Q. Sun, B. Zhang, L. Diao, B. Chen, K. Song, L. Ma and F. He, *J. Mater. Chem. A*, 2020, **8**, 11607–11616.
13 Q. Zhang, S. Tan, R. G. Mendes, Z. Sun, Y. Chen, X. Kong, Y. Xue, M. H. Rümmeli, X. Wu and S. Chen, *Adv. Mater.*, 2016, **28**, 2616–2623.
14 Q. Zhang and L. Fu, *Chem*, 2019, **5**, 505–525.
15 Q. Q. Pang, Z. L. Niu, S. S. Yi, S. Zhang, Z. Y. Liu and X. Z. Yue, *Small*, 2020, **16**, 2003007.
16 K. Wu, B. Chen, S. Yang, G. Wang, W. Kong, H. Cai, T. Aoki, E. Soignard, X. Marie and A. Yano, *Nano Lett.*, 2016, **16**, 5888–5894.
17 Y. Zhao, J. Li, J. Huang, L. Feng, L. Cao, Y. Feng, Z. Zhang, Y. Xie and H. Wang, *Adv. Mater. Interfaces*, 2020, **7**, 2001196.

18 G. Kim, S.-M. Jung, A. Giri, J.-S. Kim, Y.-W. Kim, K.-S. Kim, D. Kim, Y. Choi, B.-J. Lee and Y.-T. Kim, *J. Power Sources*, 2023, **579**, 233287.
19 Y. Liu, H. Li, J. Li, X. Ma, Z. Cui, D. Gao and Z. Tang, *J. Mater. Chem. A*, 2021, **9**, 14451–14458.
20 A. Tahira, Z. H. Ibupoto, R. Mazzaro, S. You, V. Morandi, M. M. Natile, M. Vagin and A. Vomiero, *ACS Appl. Energy Mater.*, 2019, **2**, 2053–2062.
21 S. Nong, W. Dong, J. Yin, B. Dong, Y. Lu, X. Yuan, X. Wang, K. Bu, M. Chen and S. Jiang, *J. Am. Chem. Soc.*, 2018, **140**, 5719–5727.
22 J. X. Feng, H. Xu, Y. T. Dong, X. F. Lu, Y. X. Tong and G. R. Li, *Angew. Chem., Int. Ed.*, 2017, **56**, 2960–2964.
23 D. C. Nguyen, T. L. L. Doan, S. Prabhakaran, D. T. Tran, D. H. Kim, J. H. Lee and N. H. Kim, *Nano Energy*, 2021, **82**, 105750.
24 Y. Chen, Y. Wang, L. Zheng, Y. Chang, S. Xu, Y. Wu, W. Zhou, Y. Lu, J. Wang and H. Li, *Mater. Today Energy*, 2022, **27**, 101042.
25 E. Oakton, D. Lebedev, M. Povia, D. F. Abbott, E. Fabbri, A. Fedorov, M. Nachtegaal, C. Copéret and T. J. Schmidt, *ACS Catal.*, 2017, **7**, 2346–2352.
26 M. Nie, H. Sun, J. Liao, Q. Li, Z. Xue, F. Xue, F. Liu, M. Wu, T. Gao and L. Teng, *Int. J. Hydrogen Energy*, 2021, **46**, 6441–6447.
27 C. Park, E. Lee, G. Lee and Y. Tak, *Appl. Catal., B*, 2020, **268**, 118414.
28 S.-H. You, S.-M. Jung, K.-S. Kim, J. Lee, J. Park, H. Y. Jang, S. Shin, H. Lee, S. Back and J. Lee, *ACS Energy Lett.*, 2023, **8**, 2201–2213.
29 J. Sun, L. Liu and F. Yang, *Appl. Catal., B*, 2022, **308**, 121215.
30 J. Park, S. Kim, G. Lee and J. Choi, *ACS Omega*, 2018, **3**, 10205–10210.
31 Y. Xu and G. Zangari, *Coatings*, 2021, **11**, 931.
32 P. Si, Z. Zheng, Y. Gu, C. Geng, Z. Guo, J. Qin and W. Wen, *Materials*, 2023, **16**, 3864.
33 R. R. Mishra and A. K. Sharma, *Composites, Part A*, 2016, **81**, 78–97.
34 L. Wang, Z. Sofer, J. Luxa, D. Sedmidubský, A. Ambrosi and M. Pumera, *Electrochem. Commun.*, 2016, **63**, 39–43.
35 Y. Zhou, E. Song, J. Zhou, J. Lin, R. Ma, Y. Wang, W. Qiu, R. Shen, K. Suenaga and Q. Liu, *ACS Nano*, 2018, **12**, 4486–4493.
36 M. Aparna and R. Chatanathodi, *ACS Appl. Nano Mater.*, 2022, **5**, 2385–2394.
37 W. H. Lee, Y.-J. Ko, J. H. Kim, C. H. Choi, K. H. Chae, H. Kim, Y. J. Hwang, B. K. Min, P. Strasser and H.-S. Oh, *Nat. Commun.*, 2021, **12**, 4271.
38 G.-Y. Kim, J. Lee, Y.-J. Rho, W.-H. Kim, M. Kim, J.-H. Ahn and W.-H. Ryu, *Chem. Eng. J.*, 2022, **446**, 136951.
39 S. M. Jung, Y. Kim, B. J. Lee, H. Jung, J. Kwon, J. Lee, K. S. Kim, Y. W. Kim, K. J. Kim and H. S. Cho, *Adv. Funct. Mater.*, 2024, 2316150.
40 B. Martín-García, D. Spirito, S. Bellani, M. Prato, V. Romano, A. Polovitsyn, R. Brescia, R. Oropesa-Nuñez, L. Najafi and A. Ansaldo, *Small*, 2019, **15**, 1904670.
41 Y. Liu, J. Li, W. Huang, Y. Zhang, M. Wang, X. Gao, X. Wang, M. Jin, Z. Hou and G. Zhou, *ACS Appl. Mater. Interfaces*, 2020, **12**, 33586–33594.
42 C. Pei, M. C. Kim, Y. Li, C. Xia, J. Kim, W. So, X. Yu, H. S. Park and J. K. Kim, *Adv. Funct. Mater.*, 2023, **33**, 2210072.
43 K.-R. Yeo, K.-S. Lee, H. Kim, J. Lee and S.-K. Kim, *Energy Environ. Sci.*, 2022, **15**, 3449–3461.
44 J. F. Callejas, C. G. Read, C. W. Roske, N. S. Lewis and R. E. Schaak, *Chem. Mater.*, 2016, **28**, 6017–6044.
45 B. Zhang, X. Zheng, O. Voznyy, R. Comin, M. Bajdich, M. García-Melchor, L. Han, J. Xu, M. Liu and L. Zheng, *Science*, 2016, **352**, 333–337.
46 C. C. McCrory, S. Jung, J. C. Peters and T. F. Jaramillo, *J. Am. Chem. Soc.*, 2013, **135**, 16977–16987.
47 S.-A. Park, K.-S. Kim, H. D. Jung, S.-M. Jung, Y. H. Moon, S. Back and Y.-T. Kim, *ACS Appl. Energy Mater.*, 2021, **4**, 4173–4180.

 